High-Performance and Durable Alcohol-Fueled Symmetrical Solid Oxide Fuel Cell Based on Ferrite Perovskite Electrode

Bangxin Li [a,b], John T.S. Irvine [a,c], Jiupai Ni [a,b], and Chengsheng Ni [a,b,*]

[a] *College of Resources and Environment, Southwest University, Chongqing 400716, China*

[b] *National Base of International S&T Collaboration on Water Environmental Monitoring and Simulation in Three Gorges Reservoir Region, Chongqing 400716, China*

[c] *School of Chemistry, University of St Andrews, North Haugh, Fife, KY16 9ST, UK*

Corresponding author: C.Ni.: nichengsheg@swu.edu.cn

KEYWORDS: ceria, ethanol, Fe-Ni alloy, exsolution, coke deposition, catalysis, solid oxide fuel cell

ABSTRACT: A solid oxide fuel cell utilizing bio-fuels such as methanol and ethanol could provide a carbon-neutral electricity generation and facilitate its applications in transport or stationary power unit. Herein, Ce^{4+} doping in $SrFe_{0.95}Ni_{0.05}O_3$ imparts $FeNi_3$ exsolution and CeO_2 precipitation in a reducing condition, contributing to the fuel reforming, C-C bond cleavage and coke consumption in the anode chamber. The ferrite perovskites are stable in ethanol/steam at 800 °C, whereas they are unstable in ethanol vapor with the high C fugacity inducing the formation of Fe^0 and carbides. However, the $Ce_{0.2}Sr_{0.8}Fe_{0.95}Ni_{0.05}O_3$ anode maintains mostly the perovskite and is free from coke after the 300 hours' operation under C_2H_5OH fuel at 0.5 V or 0.7 V because of the dynamic balance between the carbon deposition and consumption since an operation for 10 hours shows a clear carbon deposition. A maximum power density of 0.58 W cm^{-2} and a polarization resistance of 0.21 Ω cm^2 at 800 °C can be obtained for the symmetrical solid oxide fuel cell with identical $Ce_{0.2}Sr_{0.8}Fe_{0.95}Ni_{0.05}O_3$ cathode and anode under an ethanol fuel. The results demonstrate that the reversible and stable $SrFeO_3$ with Ce/Ni co-doping has a bright prospect for alcohol fuel oxidation.

1. Introduction

Solid oxide fuel cells (SOFCs) are promising energy-generation devices for converting chemical energy into electricity with higher efficiency than conventional heat-engine plants [1]. SOFC normally operates at high temperature from 500 to 1000 ºC and direct utilizes hydrogen [2], gaseous carbonaceous fuels [3] and liquid alcohols like methanol [4] and ethanol [5]. Hydrogen fuel is an ideal candidate for SOFC, but the major obstacle to the widespread use of hydrogen in fuel cells lies in the premature infrastructure for the storage and distribution of the hydrogen fuel [6]; *i.e.* utilizing hydrocarbons to generate electricity has been drawn great attention to commercialization because of their easier storage and distribution than H_2 [7]. Over the last few decades, there has been a steadily growing demand for the biomass hydrocarbon due to climate change [8]. The efficient utilization of energy from biomass is one of the most important ways to achieve carbon neutrality [9]. Liquid methanol and ethanol can be produced directly from renewable biomass and solar energy and have been considered as the most promising fuel for commercial utilization at ambient pressure [10].

Within the anode, the ethanol fuel reforming produces small molecules, such as carbon monoxide and hydrogen, to reduce the complexity of the prior fuel processing systems [11]. Albeit ethanol conversion is thermodynamically high at typical working temperatures of SOFC [12], there are still various issues to be tackled regarding the coke deposition on the anode side as the insufficient cleavage of C-C bond in the C_2 fuel favors the carbon deposition reaction [13].

The state-of-the-art nickel cermet anode for SOFC is efficient in H_2 oxidation but is unstable in carbonaceous fuel as a result of coking, and thus various oxide anode structures and materials of an SOFC were designed to combine the cracking of molecules and the electricity generation [14]. For example, rational structure design strategies including the integration of a porous electrolyte [15] and hierarchically porous anode [16, 17] has been employed to boost the coke resistance of the cells.

Compared with Ni(O) cermet, perovskite oxide with a nominal formula ABO_3 (A = rare-earth or alkaline-elements, B = transition elements) is much better at suppressing coking and carbon deposition [18], and makes it possible to utilize in symmetrical solid oxide fuel cell (SSOFC) with identical cathode and anode which could solve the problems of coking and sulfur poisoning by switching between the anode and cathode [19]. Metal particles on the surface of oxide anode was employed to enhance the performance for fuel internal oxidation: a small amount of Ni particles exhibiting high C–

C cleavage activity under ethanol fuel can be used for production of CO or H_2 [20], while the accumulated carbon on the anode can be removed in the re-oxidation of the anode since the volumetric expansion of dispersed Ni^0 on oxide during the re-oxidation was too minor to cause the failure of the stack [21]. The oxide anode can be metallized through ionic impregnation [22], the exsolution of metal or alloy particles of reducible cations, such as Co^{2+}, Pt^{2+} and Ru^{4+} from oxide anodes, upon exposure to fuel, was able to yield well-dispersed metallic nano-particles for more active sites [23]. Moreover, the carbon formation can be suppressed by decreasing the size of the metals or alloys: *e.g.* metal particles smaller than 7 nm or Ni alloying with Fe [24], Sn [25]and Co [26] were found to reduce the coke deposition during the steam reforming of ethanol.

Although the well-designed oxide/metal composite anode can be used to withstand the coking process to some extent, the final oxidation of the fuel/coke requires the oxygen from the cathode to complete the reaction cycle in a long-term operation. Here, we demonstrate how compositing a ferrite perovskite based on $SrFeO_3$ with an appropriately with Ni^{2+} doping on the B site and excessive Ce^{4+} on the A site was reduced to drive the superficial exsolution of Fe-Ni alloy as co-catalyst and makes it possible to tune the overall coke deposition of the anode electrode and to mediate, or even fully eliminate. The dynamic situation of coke deposition under different environment is also known to demonstrate the coke behavior upon heating over a certain range of temperatures. $Ce_{0.2}Sr_{0.8}Fe_{0.95}Ni_{0.05}O_3$ perovskite oxide as electrode **(Scheme 1)** was pre-reduced and the interaction between the electrode with combined metal/CeO_2 particles and ethanol was subjected to carbon deposition and anode decomposition under an open circuit voltage condition, while a continuous electricity output with decent electrode stability could be maintained at 0.5 V or o.7 V under an SOFC mode. This work provides significant insights into the design and operation of a long-term operating with controllable coke deposition alcohol-fueled SOFC with ferrite electrode for both cathode and anode.

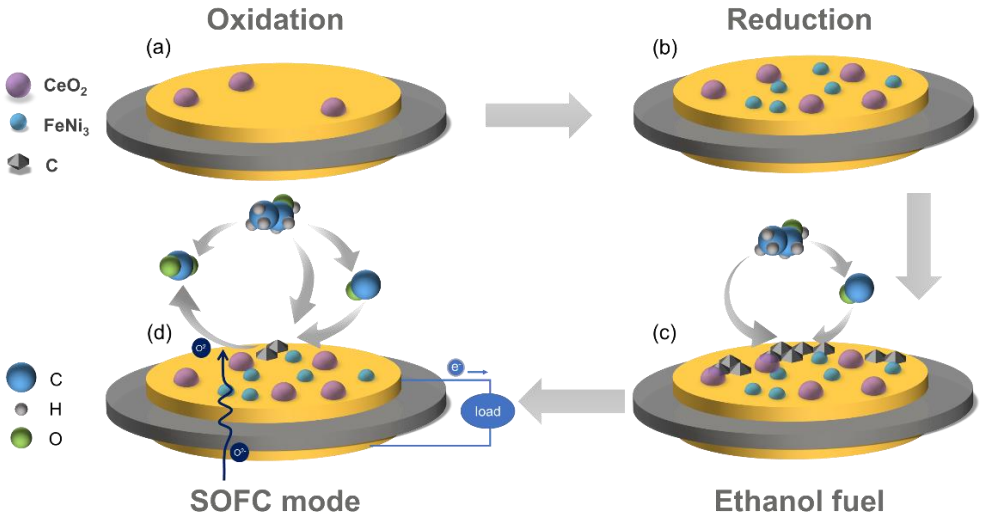

Scheme 1. Schematic diagrams of oxide anode with ceria and exsolved Fe-Ni alloy for continuous and robust ethanol oxidation. Ferrite oxide with ceria on the surface (a), alloy and ceria exsolution after reduction in hydrogen (b), carbon deposition under ethanol fuel without steam at an open circuit voltage condition (OCV) (c), and ethanol fuel oxidation underload in a fuel cell mode (d).

2. Experimental section

2.1 Materials preparation

$SrFeO_3$ (SF), $Ce_{0.1}Sr_{0.9}FeO_3$ (Ce10SF), $Ce_{0.15}Sr_{0.85}FeO_3$ (Ce15SF), $Ce_{0.2}Sr_{0.8}FeO_3$ (Ce20SF), $SrFe_{0.95}Ni_{0.05}O_3$ (SFN), $Ce_{0.1}Sr_{0.9}Fe_{0.95}Ni_{0.05}O_3$ (Ce10SFN), $Ce_{0.15}Sr_{0.85}Fe_{0.95}Ni_{0.05}O_3$ (Ce15SFN), and $Ce_{0.2}Sr_{0.8}Fe_{0.95}Ni_{0.05}O_3$ (Ce20SFN) were prepared by a combustion method. Precursors with stoichiometric ratios of $Ce(NO_3)_3{\cdot}9H_2O$ (99.9%, Macklin, China), $SrCO_3$ (99.9%, Macklin, China), $Fe(NO_3)_3{\cdot}9H_2O$ (99.9%, Aladdin, China) and $NiC_4H_6O_4{\cdot}9H_2O$ (99.9%, Macklin, China) were dissolved in de-ionized water where equal molar citric acid (CA) to the cations was added. The solution was constantly stirred until they were gel states and calcined at 600 and 1250 °C for 5 hours.

2.2 Characterization

The crystal phases were determined using X-ray diffraction (XRD) on a monochromated Persee XD-3 diffractometer with a Cu cathode ($K_{\alpha1}$ = 1.5406 Å). Thermogravimetric (TG) analyses in Ar-5% H_2 were carried out on 25 mg sample under flowing (25 mL min^{-1}) Ar-5% H_2 or synthetic air (TG209

F3 tarsus, NETZSCH, Germany). Hydrogen temperature-programmed reduction (H_2-TPR) and temperature-programmed oxidation (TPO) of the oxidized and carbonized samples under ethanol vapor were performed on a chemisorption device (VDSorb-9li, Vodo, China) equipped with a thermal conductivity detector in the temperature range from 30 to 900 ºC (10 ºC min^{-1}) in a flow (15 sccm) of Ar-5% H_2 and synthetic air for H_2-TPR and TPO, respectively. The H_2 consumption was calibrated against that of 0.005 g CuO. The electrical conductivity was measured using a high-accuracy multi-meter (Keithley 2100, USA) using the four-probe method in flowing (30 mL min^{-1}) air during the heating and Ar-5% H_2 during the cooling. The thermal expansion coefficient (TEC) of Ce20SF and Ce20SFN was measured on a dilatometer (PCY–1400II, Xiangtan, China) during the heating in air and Ar-5% H_2 in the temperature range from 25 to 800 ºC. The length of the bar for TEC was around 20 mm and the ramp rate of heating was 5 ºC min^{-1}. 100 mg of the as-prepared or reduced Ce20SFN was filled in a U-tube using quartz wool to make a bad. The ethanol reforming process was carried out heating from 20 to 800 ºC with a flowing Ar bubbled through H_2O and ethanol at 25 ºC to achieve a gas mixture containing 2.5 vol. % H_2O and 1 vol. % ethanol vapor, respectively. The efflux in ethanol reforming and TGA was analyzed a HIDEN QIC-20 instrument for the H_2 and CO_2 concentration at m/e = 2 and 44, respectively. X-ray photoelectron spectroscopy (XPS) was obtained on a Thermo ESCALAB 250Xi spectrophotometer equipped with a 150W Al K_α radiation. The morphologies were examined using SEM (ZEISS SUPRA 55) with energy dispersive spectroscopy (EDS, Bruker).

2.3 Electrochemical measurement

Ce20SF and Ce20SFN powders were refined by ball-milling and then mixed with a vehicle containing polyvinyl butyral in terpineol to prepare a slurry that would be painted onto both surfaces of an $La_{0.9}Sr_{0.1}Ga_{0.8}Mg_{0.2}O_{3-\delta}$ (LSGM) disk (10 mm in diameter, 0.3 mm in thickness). The green film was dried at 80 ºC and then calcined at 1100 ºC for 2 h. Ag containing 20 wt. % starch was also painted on the surface of both electrodes to collect the current over an active area of 0.15 - 0.2 cm^2. The anode was reduced in Ar-5% H_2 for 2 hours before the introduction of alcohol fuel to the anode while the cathode was exposed to ambient air. A flowing Ar (30 mL min^{-1}) bubbled through C_2H_5OH or CH_3OH liquid carried the fuel into the anode chamber and the actual flow rate of fuel was calculated based on the saturation vapor pressure. The current density-voltage (I-V) curves and electrochemical impedance spectroscopies (EIS) of the symmetrical cell were measured in the frequency range of 0.1 - 1 MHz

with a sinewave of 10 mV.

3. Results

3.1 Ceria doping and metal exsolution

Ce10SFN showed a monophasic perovskite similar to SFN **(Figure 1(a))**, while Ce15SFN and Ce20SFN maintained perovskite phases with minor CeO_2. A good chemical compatibility **((Figure S1))** was found between LSGM and Ce20SFN according to the XRD of their admixture calcined at 1100 ºC in air. According to the XRDs **(Figure 1(b))**, SFN decomposed to $Sr_2Fe_2O_5$ structure after the reduction in 5% H_2 at 800 ºC, while Ce doped samples maintained the perovskite structure. The reduction process in 5% H_2 enlarged the cell volume of Ce20SFN and Ce15SFN **(Table S1)** expanded by 4.2% and 4.8% and drove the exsolution of $FeNi_3$ phase as a result of Ni doping since no metal exsolution was found in Ce20SF **(Figure S2)**. The CeO_2 peak for Ce20SFN **(Figure 1(c))** in oxygenated state located at 28.72º, but after the reduction it shifted to higher angle at 28.54º as a result of the cell expansion from 4.8485 Å to 4.8828 Å. The shift of CeO_2 peak after reduction could be related to the transition from Ce^{4+} to Ce^{3+}. The relative peak intensity of CeO_2 increased after the reduction, which could be related to the exsolution of $FeNi_3$ alloy **(Figure 1(d))** that increased the A/B ratio in the perovskite. SEMs of Ce20SFN and Ce20SFN-R **(Figure 1(e, f))** confirmed that $FeNi_3$ nanoparticles of 100 nm in diameter (a population density of 27 μm^{-2}) socketed homogeneously on the surface. The Fe-Ni alloy on the surface was found to be produced in the sequential exsolution and alloying process and was facilitated by the partial Ni on the Fe site of the perovskite [27].

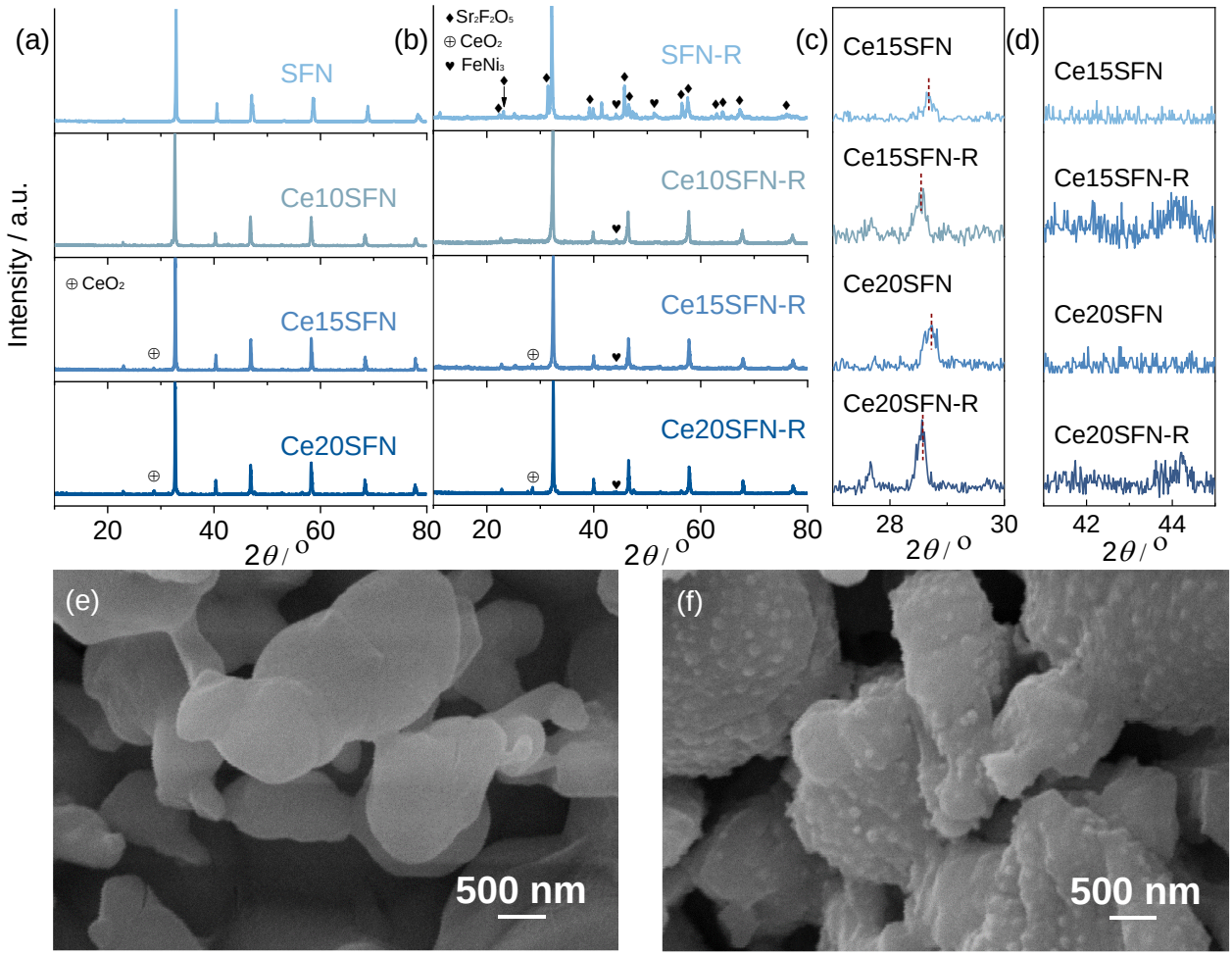

Figure 1. XRDs of SFN, Ce10SFN, Ce15SFN and Ce20SFN before (a) and after (b) reduction; the magnified CeO_2 peaks between 27° and 30° and $FeNi_3$ peaks between 41° and 45° are highlighted in (c) and (d), respectively. SEMs of Ce20SFN powders before (e) and after (f) reduction at 800 °C in Ar-5% H_2 for 5 h.

Ce10SFN without superficial CeO_2 showed the lowest weight loss amongst the four samples **(Figure 2(a))**. The dTG peaks at 270 °C of SFN and Ce10SFN could be related to the transition of Ni^{3+} to Ni^{2+} and the absence of this peak in Ce15SFN and Ce20SFN indicated that Ni was in a divalent state as a result of Ce^{4+} doping [28]. The two emerged TPR peaks **(Figure 2(b))** located from 400 °C to 600 °C represented the transition from Fe^{4+} to Fe^{3+} in perovskite-type structure [29] and the peak at 790 °C could be ascribed to the production of Fe^{2+} along with the exsolution of Fe-Ni alloy. Because ceria showed a TPR peak at a temperature higher than 800 °C **(Figure S3)**, the increased Ce^{4+} content in Ce10SFN, Ce15SFN and Ce20SFN could decrease the Fe^{4+} content in the initial oxides for the charge neutrality [30, 31]. However, Ce15SFN and Ce20SFN with ceria exsolution showed higher

oxygen storage capacity (OSC) than Ce10SFN in terms of H_2 consumption and weight loss in 5% H_2 **(Figure 2(c))**. Higher Ce^{4+} doping in Ce15SFN and Ce20SFN could increase the initial oxygen content in the as-prepared perovskite or the oxide-ion conduction in the perovskite as can be seen from their higher H_2 consumption below 500 °C than Ce10SFN.

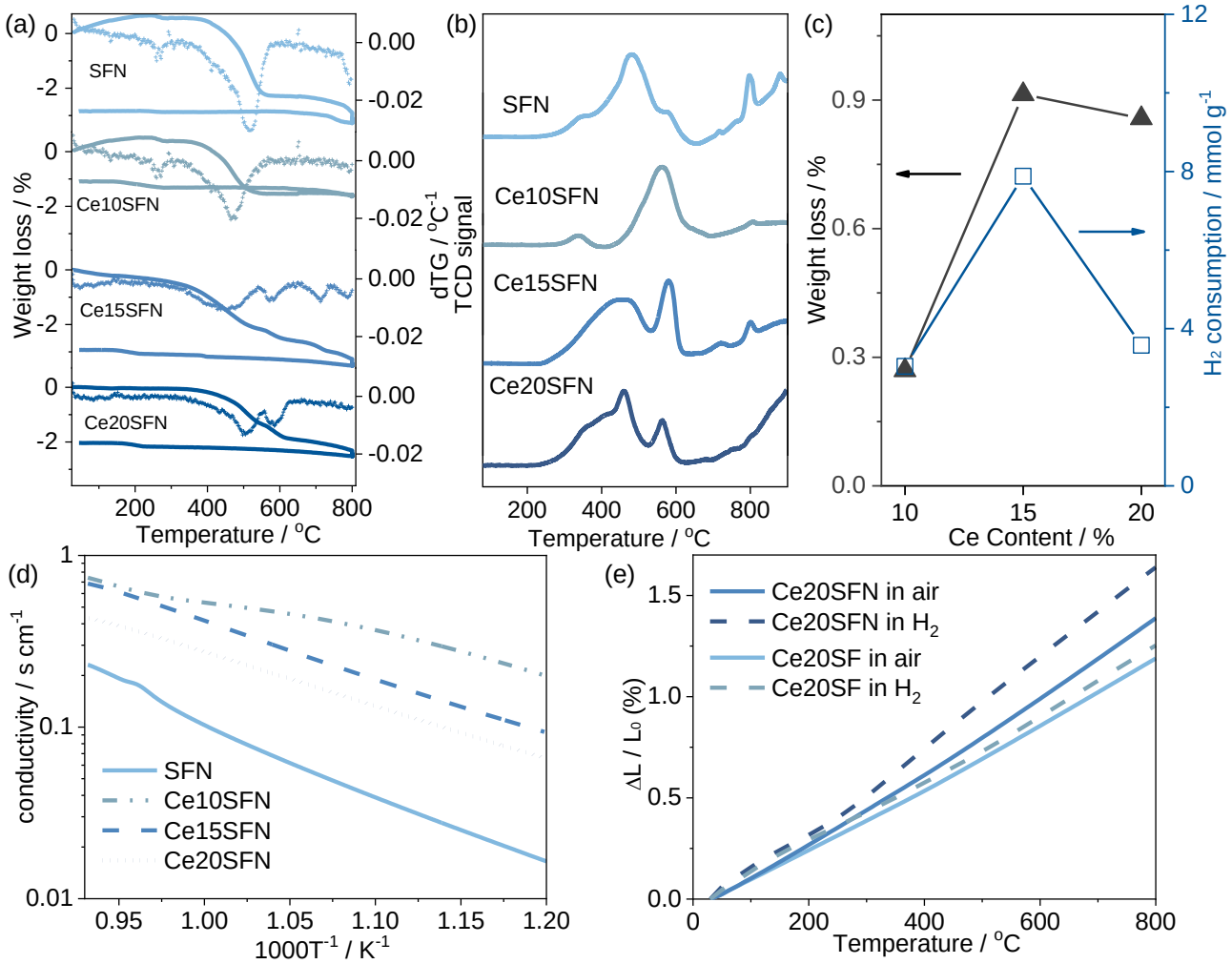

Figure 2. (a) TGA and (b) TPR of SFN, Ce10SFN, Ce15SFN and Ce20SFN in 5% H_2. The mass loss and dTG during the heating in (a) are solid and dashed lines, respectively. (c) The oxygen storage capacity (OSC) of Ce10SFN, Ce15SFN and Ce20SFN in terms of weight loss in TGA and H_2 consumption in TPR. (d) Temperature dependence of electronic conductivity of SFN, Ce10SFN, Ce15SFN and Ce20SFN samples after 5 hours' reduction under 5% H_2 flow during the cooling times. (e) Thermal expansion of Ce20SFN and Ce20SF in air and 5% H_2 from 40 to 800 °C, respectively.

The electrical conductivity **(Figure 2(d))**, σ, of SFN, Ce10SFN, Ce15SFN and Ce20SFN

showed a semiconducting behavior in 5% H_2, indicating that the oxides rather than the exsolved alloy were responsible for the electric conductivity. The σ of Ce10SFN (0.74 S cm^{-1}), Ce15SFN (0.68 S cm^{-1}) and Ce20SFN (0.42 S cm^{-1}) at 800 ºC were much higher than undoped SFN (0.23 S cm^{-1}) as Ce^{4+} doping increased the stability the structure during reduction [32-34]. The isothermal conductivity **(Figure S4)** of Ce10SFN, Ce15SFN and Ce20SFN at 800 ºC showed a valley with time as a result of the conductivity transition from *p*-type conductivity for $Fe^{4+/3+}$ to *n*-type for $Fe^{3+/2+}$ [35]. TEC **(Figure 2(e))** of Ce20SFN in air was 17.81 ppm K^{-1}, which was smaller than $SrFeO_3$ (40.80 ppm K^{-1}) and $SrFe_{0.8}Mo_{0.2}O_3$ (25.70 ppm K^{-1}) [36]. The TEC of the reduced Ce20SFN increased to 21.03 ppm K^{-1}, which was higher than Ce20SF in hydrogen (16.13 ppm K^{-1}).

3.2 H_2 evolution under steam reforming

The ethanol steam reforming involved several competing reactions dependent on temperature and pressure. Dehydrogenation of ethanol was confined mainly to the temperature range below 400 ºC for the product acetaldehyde, H_2, and small amounts of CO and CH_4. Ce20SFN-R with Fe-Ni alloy **(Figure 3(a))** showed a lower starting temperature than Ce20SFN for the production of H_2. On the other hand, the ethanol and hydrocarbons reforming was predominant above 400 ºC for the production of more H_2 and CO [37]. The exsolved CeO_2 with higher oxygen mobility favored the reforming of hydrocarbon with steam, leading to maximization of hydrogen production. The further increase in temperature (above 600 ºC) could decrease the H_2 concentration as a result of the reverse water-gas shift reaction (RWSR) [38]. Ce20SFN and Ce20SFN-R after ethanol reforming with water both remained mostly as perovskite **(Figure 3(b))**, but the former showed a minor $SrCO_3$ phase because of the redundant accumulation of acetaldehyde on the surface causing the decomposition of perovskite due to the carburizing process.

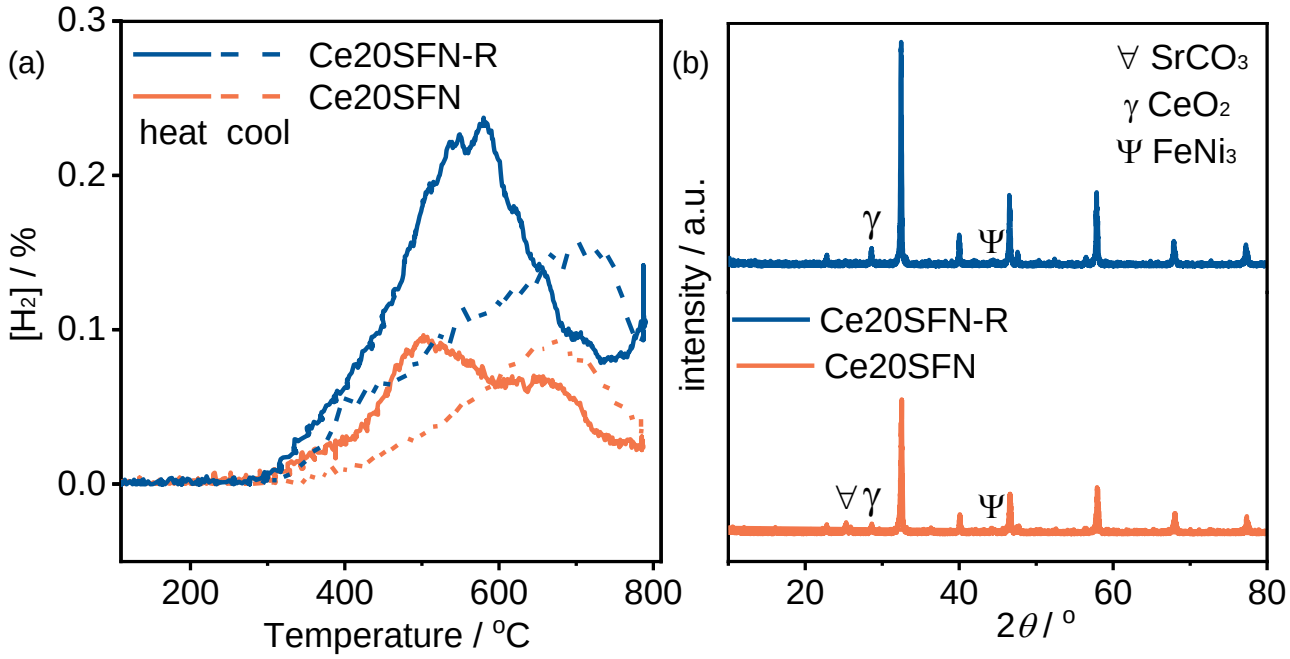

Figure 3. (a) Hydrogen concentration under ethanol steam reforming in the fixed-bed reactor from 20 to 800 °C over Ce20SFN and Ce20SFN-R during the heating (solid lines) and cooling (dashed lines). (b) XRD of Ce20SFN and Ce20SFN-R after catalysis measurement.

Carbon formation seemed to be unavoidable for most hydrocarbon fuels in the temperature ranges between 20 and 800 °C [39]. Although Ce20SF and Ce20SFN were stable in H_2 at 800 °C, the oxygen partial pressure may not be the only parameter for the decomposition and reduction process. Since carbon deposition was possible and according to the Fe-C-O phase diagram **(Figure S5)**, the trace deposition of C at the beginning would induce the formation of FeC_x at an oxygen partial pressure ($P(O_2)$) higher than that for the production of Fe^0. The formation of carbides was found to be efficient in catalyzing the further deposition of carbon. In order to study the effect of surface variation on the carbon deposition under ethanol vapor, Ce20SF(N) with or without the prior reduction annealed under ethanol vapor for 5 hours showed decomposition in ethanol vapor at 800 °C according to the XRDs **(Figure 4(a))**: *i.e.*, the perovskite oxide with or without prior reduction decomposed completely into Fe^0 along with some Sr_2CeO_4, CeO_2, $SrCO_3$, C and FeC_x.

The deposition of C or formation of FeC_x can be confirmed by the re-oxidation of the residue during the TPO measurement **(Figure 4(b))**. The TPO signals below 100 °C could be related to the loss of absorbed water or ethanol as weight loss was shown in the TG **(Figure 4(c))**. The peak at 500

ºC could be assigned to the FeC_x oxidization (~500 ºC) because more oxygen was consumed than the released CO_2, whereas the one at 600 ºC corresponded to the oxidation of carbonaceous material (~600 ºC) for the production of large amount of CO_2 [40].

The weight gain **(Figure 4(c))** of the samples aged under ethanol vapor started at around 250 ºC as a result of the oxidation of Fe^0 or oxides and carbides, and the weight loss after 500 ºC could be related to the oxidation of C as CO_2 was found in the efflux. According to the CO_2 signal **(Figure 4(d))** in TPO, Ce20SF without metal exsolution accumulated less carbon than Ce20SF-R because the initial reduction would decrease the OSC that was required for the oxidation of ethanol and increased the possible deposition of carbonaceous species [41]. In contrast, Ce20SFN-R showed less carbon deposition than Ce20SFN since the exsolved CeO_2 with Fe-Ni alloy would benefit from the partial oxidation of ethanol for the gaseous product, such as acetaldehyde or ethylene, to avoid the deposition of carbon.

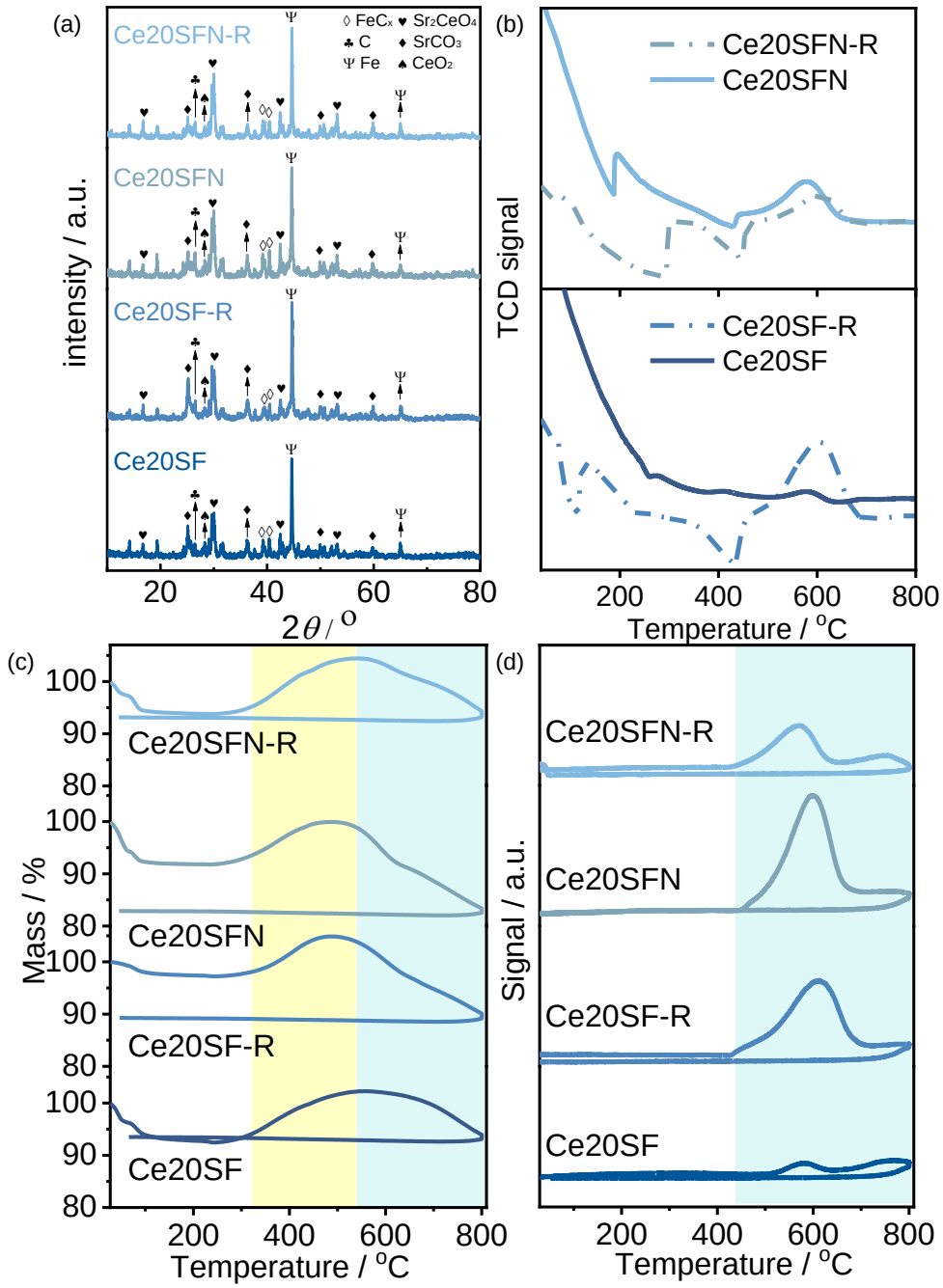

Figure 4. (a) XRDs, (b) TPO and (c) TGA in air for Ce20SF, Ce20SF-R, Ce20SFN and Ce20SFN-R after the aging under ethanol vapor without steam at 800 °C. (d) The corresponding signal of *m/e*=44 in the efflux of TGA in air.

XPS **(Figure 5(a))** was carried out to confirm the elemental composition and valence states of Ce20SFN, Ce20SFN-R and Ce20SFN-R-F (Ce20SFN-R annealed under ethanol vapor). The Ce 3d spectrum **(Figure 5(b))** with multiple splits could be split for ceria species of Ce^{3+} and Ce^{4+}, respectively. However, the characteristic peak for Ce^{4+} at 916.2 eV decreased and the peak of Ce^{3+} at

880.9 eV showed more obvious for the reduced sample. Ce^{3+} with a similar ionic radius similar to La^{3+} could be on A site, but Ce^{4+} can also be on B site of a perovskite (*e.g.* as in $SrCeO_3$) and causing A-site deficiency. The Ce^{4+} substitution on the Fe site would increase the lattice volume of Ce10SFN than SFN since its ionic radius (87.0 pm) is much larger than those of Fe ions (Fe^{4+} for 58.5 pm *v.s.* Fe^{3+} for 64.5 pm) **(Table S1)**. Since the A-site deficient tolerance of a perovskite increases with the bond energy of <B-O> [42, 43], Ni doping on Fe site decreasing the <B-O> bond energy, which is in accord with the fact that Ce15SF did not show a CeO_2 secondary phase, but Ce15SFN did. The superficial cation composition according to the XPS scan **(Table S2)** indicates that Ce20SFN or Ce20SFN-R was A-site excess, and specifically the $Ce^{4+/3+}$ concentration decreased because of the reduction of Ce^{4+} would produce Ce^{3+} that could fit better on the A-site of the perovskite.

While two asymmetric peaks were observed in the Fe 2p spectrum **(Figure 5(c))**, each of which could be decomposed into three peaks, corresponding to a mixed oxidation state of $Fe^{+2/+3/+4}$ [44]. All the peaks of Fe 2p shifted to lower binding energy along with the reduction of Fe cations [45]. The peak at 706.0 eV for exsolved Fe^0 in 5% H_2 was intensified in Ce20SFN-R-F than Ce20SFN-R [46]. Core-level scan of Ni $2p_{3/2}$ **(Figure 5(d))** for Ce20SFN could be fitted into the main peak for Ni^{2+} at 854.4 eV, but the subpeaks in Ce20SFN-R at 852.3 eV and 854.4 eV could be assigned to metallic Ni^0 and Ni^{2+}, respectively. Peaks for metallic Ni were observed in both Ce20SFN-R and Ce20SFN-R-F as a result of Ni^0 exsolution during the reduction in 5% H_2 and the following C_2H_5OH (g) flow. Moreover, the addition XPS peak at 854.0 eV for Ce20SFN-R-F indicated the presence of Ni_3C phase [47].

The C 1s spectrum **(Figure 5(e))** of Ce20SFN consisted of peak C–C (284.5 eV), C–O (286.6 eV) and C=O (288.0 eV), but the reduced one showed a higher content of C=O and the presence of C–OR (287.9 eV), which related to the absorbed polyaromatics species on the surface. The major IR-bands at 1436 cm^{-1} in Fourier transform infrared (FTIR) spectroscopy **(Figure S6)** is also assigned to the symmetrical stretching of a -COOH [48]. The O 1s spectrum **(Figure 5(f))** showed three peaks for M-O (529.0 eV), oxygen vacancy (532.0 eV) and C=O species (534.5 eV), respectively.

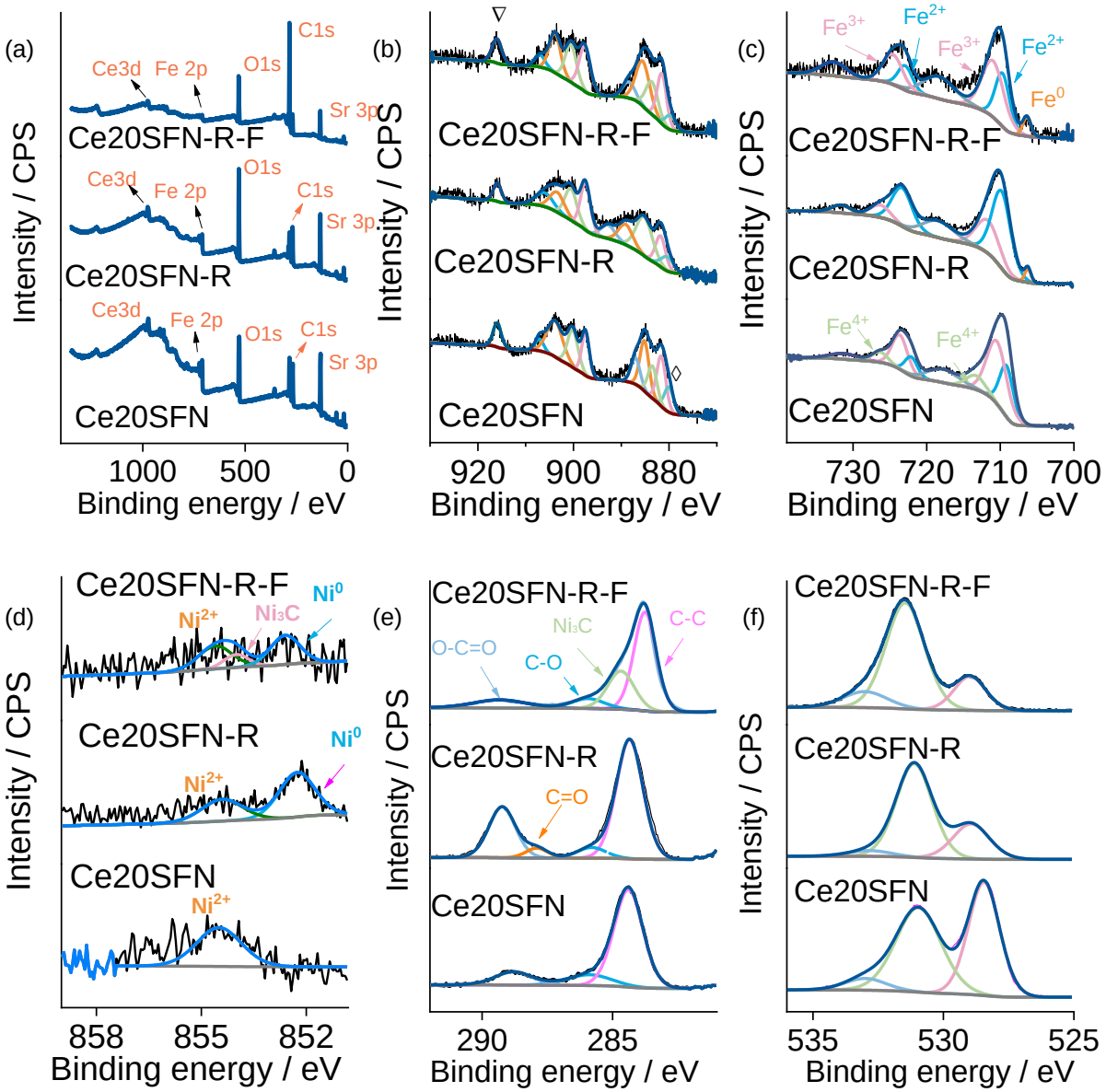

Figure 5. XPS of Ce20SFN, Ce20SFN-R, Ce20SFN-R after aging under ethanol vapor (Ce20SFN-R-F): (a) overview survey and the high-resolution core-level scans of (b) Ce 3d, (c) Fe 2p, (d) Ni $2p_{3/2}$, (e) C 1s and (f) O 1s. The triangle and diamond mark in (b) indicate the characteristic peaks for Ce^{4+} at 916.2 eV and Ce^{3+} at 880.9 eV, respectively.

3.3 Alcohol-fueled cell testing and stability

I-V curves for SSOFC based on Ce20SF and Ce20SFN under the C_2H_5OH-fuel and static air oxidant **(Figure 6(a))** indicated that the cell with Ce20SF electrode showed curvature high deactivation at 700 and 750 °C until the voltage was lower than 0.5 V. In contrast, the cell with Ce20SFN showing a quasi-linear I-V curve indicated the exsolution of Ni-Fe alloy would promote for the decomposition

and oxidation of ethanol fuel. IV curve **(Figure 6(b))** of the cells under methanol fuel showed higher current density than those under ethanol fuel.

The Ce20SFN cell under methanol fuel **(Figure 6(c))** showed peak power densities (PPDs) of 0.57, 0.45 and 0.20 W cm^{-2} at 800, 750 and 700 ºC, respectively, similar to those under ethanol fuel (0.58, 0.41, 0.18 W cm^{-2}). The PPD for Ce20SFN in 800 ºC was superior to that of $La_{0.6}Sr_{0.4}Co_{0.2}Fe_{0.7}Mo_{0.1}O_{3-\delta}$ (0.48 W cm^2 at 850 ºC in ethanol), $(La_{0.6}Sr_{0.4})_{0.9}Co_{0.2}Fe_{0.6}Nb_{0.2}O_3$ (0.062 W cm^2 at 800 ºC in ethanol), the anode supported cell with a Cu-CeO_2 impregnated Ni-YSZ support layer (0.40 W cm^2) and the other reported anode using ethanol fuel **(Table S3)** [49, 50]. However, the power densities of Ce20SF cell with ethanol (0.13, 0.12 and 0.09 W cm^{-2}) was much lower than the one in methanol (0.48, 0.22, 0.10 W cm^{-2}), which was subjected more to thermal activation in methanol than the cell in ethanol. The different behavior in cell performance for Ce20SF and Ce20SFN cell under methanol and ethanol, indicated that Ni-Fe alloy was efficient in cracking the C-C bond.

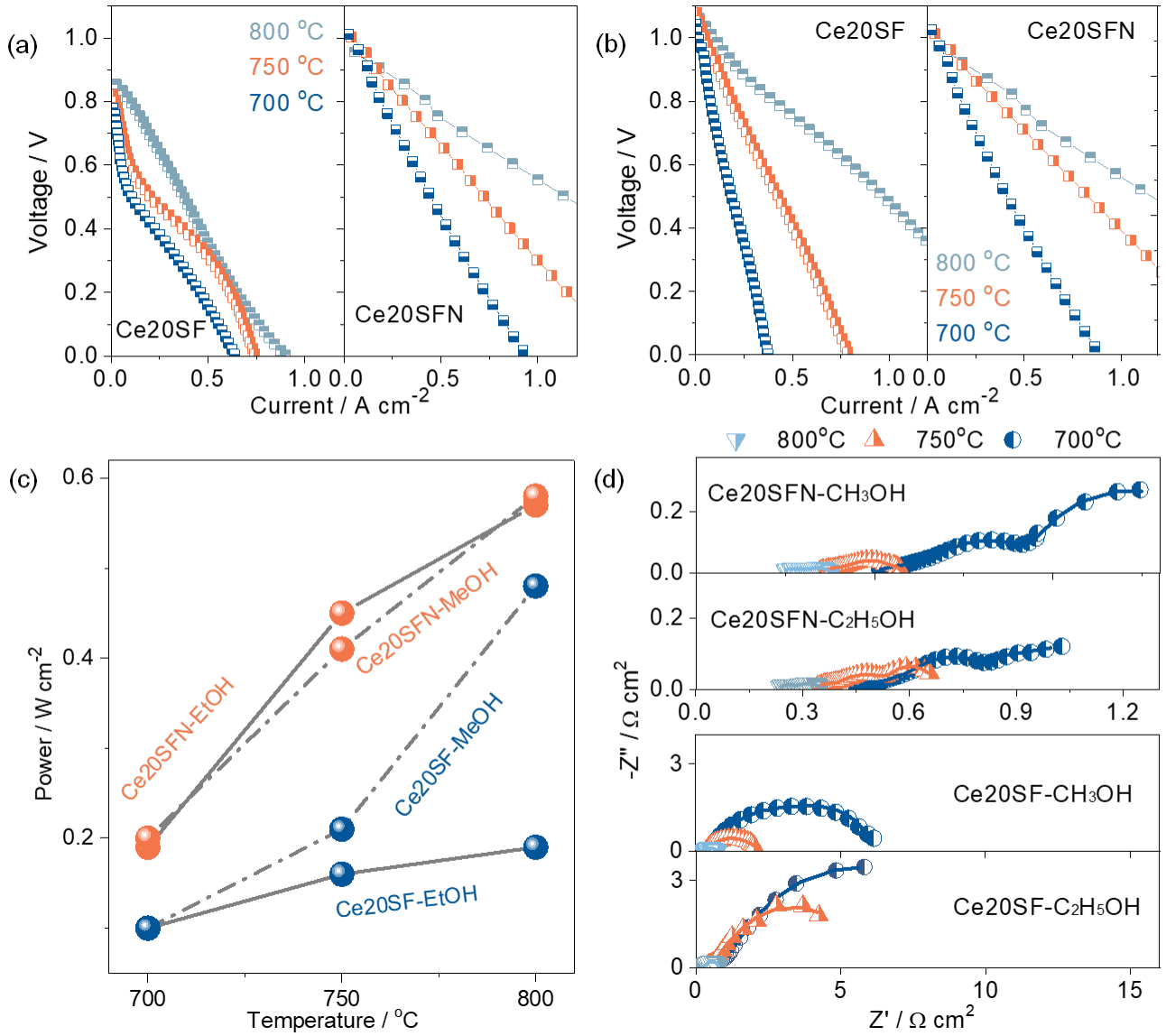

Figure 6. The IV curves of Ce20SF/LSGM/Ce20SF (left) and Ce20SFN/LSGM/Ce20SFN (right) for (a) ethanol and (b) methanol fuel at 700, 750 and 800 °C. (c) Peak power densities of Ce20SF/LSGM/Ce20SF and Ce20SFN/LSGM/Ce20SFN cells at tested temperatures in ethanol and methanol, respectively. (d) EIS of Ce20SF/LSGM/Ce20SF and Ce20SFN/LSGM/Ce20SFN with ethanol and methanol as fuel.

Three arcs could be distinguished in the EIS of the cells under alcohol fuel and air **(Figure 6(d) and Figure S7)** at OCV, where the polarization resistance (R_p) estimated from the impedance of the low-frequency end subtracting the high frequency intersection between the impedance and x-axis. Ni doping greatly reduced the magnitude of the R_p: *e.g.* the Ce20SFN cell under ethanol fuel was smaller than Ce20SF cell at 700 °C (10 Ω cm^2 versus 2 Ω cm^2). A fitting with an equivalent circuit containing

three Voigt elements would benefit the assignment of corresponding reaction steps. At 700 ºC, the fitted resistance parameter **(Figure S8)** showed that the R_3 for the low frequency dominated the R_p for Ce20SF and Ce20SFN cell at 700 ºC because of the slow gas phase diffusion of ethanol molecules. As temperature increased to 800 ºC, the proportion of R_3 in R_p (64% for Ce20SF and 54% for Ce20SFN) decreased as a result of the ethanol thermal conversion into small molecules. Besides, Ni doping in Ce20SF decreased the R_2 since the enhanced catalysis on ethanol facilitated the charge transfer process on the electrode/electrolyte interface, and thus decreased R_3 due to simultaneous production of smaller molecules on the anode. The analysis of the EIS of methanol fueled cells with Ce20SF and Ce20SFN suggested that R_2 related to the dissociation/adsorption was more important in the electrochemical than that in ethanol fuel, because the shorter carbon bond and lower molecular weight could reduce the diffusion resistance.

The current densities of the cells **(Figure 7(a))** with Ce20SF and Ce20SFN at a constant voltage of 0.5 V at 700 ºC all showed a slight variation and the current density reached 1.1 A cm^{-2} and 0.3 A cm^{-2}, respectively, after 10 hours. The variation of Ce20SFN could be related to the fluctuation of unstable flow during the feeding process. The cross-sectional microstructures of the symmetrical cells **(Figure 7(b) and (c))** clearly showed that both the anode and cathode were well anchored on the electrolyte and the thickness of Ce20SFN anode was about 60 μm. The Ce20SF and Ce20SFN anodes **(Figure 7(d) and (e))** showed matt surface with small spherical particles of 10 nm in diameter which could be the deposition situation of polyaromatics on the surface of the electrode after 10-h test.

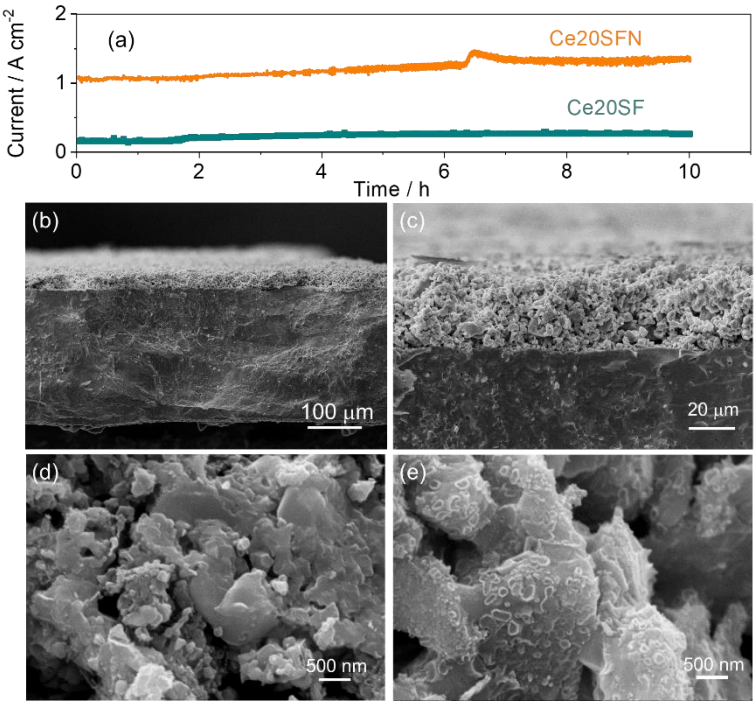

Figure 7. (a) Current density variation of the Ce20SFN and Ce20SF cell under voltage of 0.5V with C_2H_5OH fuel for 10 h. (b, c) Low-magnification SEM of Ce20SFN/LSGM/Ce20SFN after 10 hours' operation under ethanol fuel. High-magnification SEM of the Ce20SF (d) and Ce20SFN (e) anode after test for 10 h.

The cell with Ce20SFN electrode for C_2H_5OH showed a stable current density of 1.0 A cm^{-2} and 0.6 A cm^{-2} under a bias at 0.5 V and 0.7 V, respectively **(Figure 8(a))**, and no obvious carbon fiber was detected in the SEM of the electrode after 300 hours' aging **(Figure 8(b))**. The elimination of carbon was also consistent with the absence of vibrating points in the current after 300 hours' durability test. Actually, with CeO_2 and Fe-Ni alloy exsolution, Ce20SFN became a quasi-SSOFC, but the main phase was identical in the cathode and anode. The anode **(Figure S9)** maintained the main phase of perovskite with a minor phase of Fe-Ni alloy, CeO_2 and $SrCO_3$ as a result of superficial decomposition. The morphology of anode after 300 h was completely different than after 10 h and the EDS mapping **(Figure 8(c-g))** proved that a clear Ni-Fe exsolution. The significant reduction in carbon deposition was related to the high oxygen exchange rate and excellent oxidation catalysis of CeO_2 and good catalysis to C-C bond crack of Ni-Fe alloy for the initial coke deposition was eliminated under anodic polarization because of ceria/alloy composite [51].

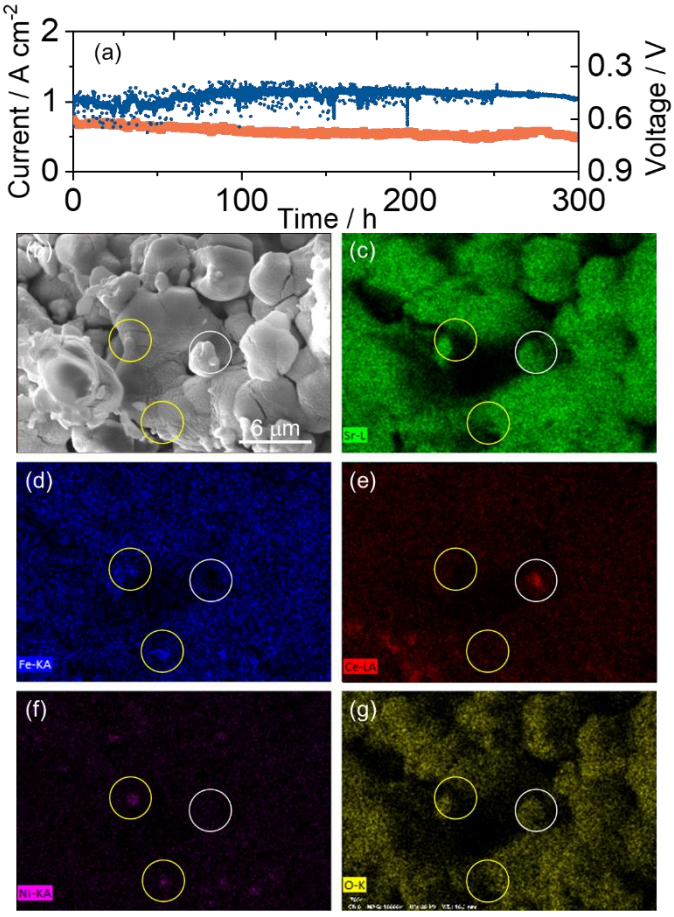

Figure 8. (a) Current density variation of the Ce20SFN cell at a voltage of 0.5V and 0.7 V during the 300-h operation under C_2H_5OH fuel. (b) SEM along with the corresponding (c-g) EDS mapping for the Ce20SFN electrode after an operation for 300 hours under a constant bias at 0.5 V. Fe-Ni alloy details are in yellow and CeO_2 in white circle.

4. Discussion

Ethanol reforming **(Equation 1)** for the production of aldehyde can be automatically conducted at a relatively low reaction temperature lower than 600 ºC [52, 53]. The scission of the C–C bond and deposition of carbon took place after the formation of acetaldehyde species, and it could be accelerated if insufficient H_2O and O_2 were provided [13]. The acetaldehyde could be finally converted into CO and a small amount of CH_4 **(Equation 2)** that induced carbon deposition through carbon monoxide disproportionation **(Equation 3)** and methane pyrolysis **(Equation 4)**.

$$2\ C_2H_5OH = 2\ C_2H_4O + H_2 \quad (1)$$

$$C_2H_4O = CO + CH_4 \quad (2)$$

$$2\ CO = CO_2 + C \quad (3)$$

$$CH_4 = C + 2\ H_2 \quad (4)$$

The carbon deposition on Ce-doped $SrFeO_3$ seems inevitable unless additional oxidant is provided for the reforming of ethanol. Ethanol could induce the loss of superficial lattice oxygen (O_O^x) of a perovskite oxide for possible production CO **(Equation 5)** and the produced $V_o^{\bullet\bullet}$ would provide the transport of oxide ion for further loss of O_O^x **(Equation 6)** [54, 55]. In this case, the formation of carbon is reduced by the gas-solid reaction of CO with the lattice oxygen for the production of CO_2 [56]. The obvious carbon deposition on Ce20SF and Ce20SFN without oxidant indicates that CH_x and CO remained on the surface and generated carbonaceous residues rather than evolved to H_2O and CO_2. Comparing with Fe^0, a reduced surface with Fe^{2+} would be more prone to induce the coke deposition [57], and this explains why the $FeNi_3$ alloy exsolved during the prior H_2 reduction does not accelerate the carbon deposition of Ce20SFN.

$$C_2H_5OH + O_O^x = 2\ CO + 3\ H_2 + V_o^{\bullet\bullet} + 2\ e' \quad (5)$$

$$CO + O_O^x = CO_2 + V_o^{\bullet\bullet} + 2e' \quad (6)$$

The decomposition of oxide perovskite could also be related to the formation of carbide that shatters the physical structure, but, fortunately, the perovskite structure could be maintained partially after the operation under bias (0.5 V) for 300 hours. Remarkably, the morphologies of the electrode after 300 hours' operation showed less carbon deposition than those after and 10 hours. The transport of O^{2-} from the cathode could act as the oxidant of ethanol for the production of H_2O and CO_2 and moreover, it can also oxidize the deposited carbon species at the OCV stage.

The wide use of ceria and ceria-based mixed oxides as an active component for catalytic oxidation in hydrocarbons reforming and water gas shift reaction (WGSR) **(Equation 7)** has been traditionally associated with the unique excellent ability of these oxides to shuttle between Ce (III) and Ce (IV) states [58, 59].

$$H_2O + CO = CO_2 + H_2 \quad (7)$$

The generation of H_2 would be beneficial for the oxidation kinetics of the fuel in the anode and increases the output of the cell. CeO_2 was found to facilitate the gasification of carbon species to partially inhibit coke formation in the presence of H_2O or CO_2, but the transport of oxygen from the cathode to the anode could be essential in this process. A dynamic balance between carbon consumption and accumulation could be achieved for a fuel cell under load. Actually, the interaction between CeO_2 and ferrite perovskite was found to strongly improve the reducibility and oxygen mobility of a perovskite [60].

5. Conclusion

A stable perovskite-type ferrite oxide Ce20SFN is explored as an electrode candidate for symmetrical solid oxide fuel cell. It exhibits outstanding reversibility and stability performance in liquid alcohol fuel condition if the cell is under a bias of 0.5 V. Trace ceria was present on the Ce20SFN and Ce20SF electrode prepared in air, but $FeNi_3$ alloy could be outgrown from the oxide lattice of Ce20SFN after the reduction in the prior hydrogen for the superior electrocatalysis of the fuel oxidation, comparing to Ce20SF. A maximum power density of 0.58 W cm^{-2} and 0.57 W cm^{-2} and an R_p of 0.13 Ω cm^2 and 0.12 Ω cm^2 can be achieved at 800 ºC for ethanol and methanol, respectively. Most importantly, the performance and structure of the SSOFC remain stable after 300 h at 0.5 or 0.7 V. The presence of CeO_2 and the in-situ exsolved $FeNi_3$ is able to remove the deposited carbon through the synergistic effect in water gas shift reaction. The studies find that $Ce_{0.2}Sr_{0.8}Fe_{0.95}Ni_{0.05}O_3$ perovskite has a bright prospect as an electrode material.

Acknowledgements

This work is supported by the NSFC (grant No. 51702264; 41371275) and National Key Research and Development Program of China (grant No. 2018FYD0200701) and research funding for central universities (XDJK2020B066). C.N. also thanks to the award of Chongqing Bayu Young Scholar from Chongqing Teaching Committee and Funding for Oversea Returnees, while J.N. thanks to the support from Chongqing Yingcai Talent.

Appendix A. Supplementary data

Unit cell parameters in Table S1; Elemental analysis by XPS in Table S2; electrochemical performance of reported SOFC with ethanol in Table S3; XRD of Ce20SFN and Ce20SF with LSGM and those before and after reduction in Figure S1 and S2; TPR for CeO_2 in Figure S4;for iso-thermal conductivity of Ce10SFN, Ce15SFN and Ce20SFN in Figure S4; phase diagram of Fe-C-O in Figure S5; FTIR spectra, the EIS in air, and fitted impedance parameters of Ce20SF and Ce20SFN in Figure S6, S7 and S8; XRD of Ce20SFN electrode in Figure S9.

Reference

[1] Minh NQ. Ceramic Fuel Cells. Journal of the American Ceramic Society. 1993;76.

[2] Stoynov Z, Vladikova D, Burdin B, Laurencin J, Montinaro D, Raikova G, et al. Differential analysis of SOFC current-voltage characteristics. Applied Energy. 2018;228:1584-90.

[3] Aslannejad H, Barelli L, Babaie A, Bozorgmehri S. Effect of air addition to methane on performance stability and coking over NiO–YSZ anodes of SOFC. Applied Energy. 2016;177:179-86.

[4] Yan D, Zhang C, Liang L, Li K, Jia L, Pu J, et al. Degradation analysis and durability improvement for SOFC 1-cell stack. Applied Energy. 2016;175:414-20.

[5] Badwal SPS, Giddey S, Kulkarni A, Goel J, Basu S. Direct ethanol fuel cells for transport and stationary applications – A comprehensive review. Applied Energy. 2015;145:80-103.

[6] Atkinson A, Barnett S, Gorte RJ, Irvine JTS, McEvoy AJ, Mogensen M, et al. Advanced anodes for high-temperature fuel cells. Nat Mater. 2004;3:17-27.

[7] Cai W, Zhou Q, Xie Y, Liu J, Long G, Cheng S, et al. A direct carbon solid oxide fuel cell operated on a plant derived biofuel with natural catalyst. Applied Energy. 2016;179:1232-41.

[8] Subotić V, Baldinelli A, Barelli L, Scharler R, Pongratz G, Hochenauer C, et al. Applicability of the SOFC technology for coupling with biomass-gasifier systems: Short- and long-term experimental study on SOFC performance and degradation behaviour. Applied Energy. 2019;256:113904.

[9] Yu F, Xiao J, Zhang Y, Cai W, Xie Y, Yang N, et al. New insights into carbon deposition mechanism of nickel/yttrium-stabilized zirconia cermet from methane by in situ investigation. Applied Energy. 2019;256:113910.

[10] Chen X, Khanna M. Effect of corn ethanol production on Conservation Reserve Program acres in the US. Applied Energy. 2018;225:124-34.

[11] Irvine JTS, Neagu D, Verbraeken MC, Chatzichristodoulou C, Graves C, Mogensen MB. Evolution of the electrochemical interface in high-temperature fuel cells and electrolysers. Nature Energy. 2016;1:15014.

[12] Neagu D, Tsekouras G, Miller DN, Ménard H, Irvine JTS. In situ growth of nanoparticles through control of non-

stoichiometry. Nature Chemistry. 2013;5:916–23.

[13] Deluga GA, Salge JR, Schmidt LD, Verykios XE. Renewable Hydrogen from Ethanol by Autothermal Reforming. Science. 2004;303:993.

[14] Chen B, Xu H, Tan P, Zhang Y, Xu X, Cai W, et al. Thermal modelling of ethanol-fuelled Solid Oxide Fuel Cells. Applied Energy. 2019;237:476-86.

[15] Xu H, Chen B, Tan P, Xuan J, Maroto-Valer MM, Farrusseng D, et al. Modeling of all-porous solid oxide fuel cells with a focus on the electrolyte porosity design. Applied Energy. 2019;235:602-11.

[16] Chen B, Xu H, Ni M. Modelling of finger-like channelled anode support for SOFCs application. Science Bulletin. 2016;61:1324-32.

[17] Connor PA, Yue X, Savaniu CD, Price R, Triantafyllou G, Cassidy M, et al. Tailoring SOFC Electrode Microstructures for Improved Performance. Advanced Energy Materials. 2018;8:1800120.

[18] Li B, He S, Li J, Yue X, Irvine JTS, Xie D, et al. A Ce/Ru Codoped $SrFeO_{3-\delta}$ Perovskite for a Coke-Resistant Anode of a Symmetrical Solid Oxide Fuel Cell. ACS Catalysis. 2020;10:14398-409.

[19] Xu HR, Chen B, Liu J, Ni M. Modeling of direct carbon solid oxide fuel cell for CO and electricity cogeneration. Applied Energy. 2016;178:353-62.

[20] Barbero BP, Gamboa JA, Cadús LE. Synthesis and characterisation of $La_{1-x}Ca_xFeO_3$ perovskite-type oxide catalysts for total oxidation of volatile organic compounds. Applied Catalysis B: Environmental. 2006;65:21-30.

[21] Lu LY, Ni CS, Cassidy M, Irvine JTS. Demonstration of high performance in a perovskite oxide supported solid oxide fuel cell based on La and Ca co-doped $SrTiO_3$. Journal of Materials Chemistry A. 2016;4:11708-18.

[22] Ni CS, Lu LY, Miller DN, Cassidy M, Irvine JTS. Microstructure dependence of performance degradation for intermediate temperature solid oxide fuel cells based on the metallic catalyst infiltrated La- and Ca-doped $SrTiO_3$ anode support. Journal of Materials Chemistry A. 2018;6:5398-406.

[23] Ni C, Zeng Q, He D, Peng L, Xie D, Irvine JTS, et al. A B-site doped perovskite ferrate as an efficient anode of a solid oxide fuel cell with in situ metal exsolution. Journal of Materials Chemistry A. 2019;7:26944-53.

[24] Lo Faro M, Reis RM, Saglietti GGA, Oliveira VL, Zignani SC, Trocino S, et al. Solid oxide fuel cells fed with dry ethanol: The effect of a perovskite protective anodic layer containing dispersed Ni-alloy @ FeO_x core-shell nanoparticles. Applied Catalysis B: Environmental. 2018;220:98-110.

[25] Farrell B, Linic S. Direct electrochemical oxidation of ethanol on SOFCs: Improved carbon tolerance of Ni anode by alloying. Applied Catalysis B: Environmental. 2016;183:386-93.

[26] Sarruf BJM, Hong JE, Steinberger-Wilckens R, de Miranda PEV. Influence of novel anode design on the performance and coke resistance towards methane directly-fed solid oxide fuel cells. Ceramics International. 2020;46:5368-79.

[27] Wu Z, Caracciolo DT, Maswadeh Y, Wen J, Kong Z, Shan S, et al. Alloying–realloying enabled high durability for Pt–Pd-3d-transition metal nanoparticle fuel cell catalysts. Nature Communications. 2021;12:859.

[28] Ni C, Zeng Q, He D, Peng L, Xie D-T, Irvine J, et al. B-site doped perovskite ferrate for efficient anode of a solid oxide fuel cell with in situ metal exsolution. Journal of Materials Chemistry A. 2019.

[29] Falcón H, Barbero JA, Alonso JA, Martínez-Lope MJ, Fierro JLG. $SrFeO_{3-\delta}$ Perovskite Oxides: Chemical Features and Performance for Methane Combustion. Chemistry of Materials. 2002;14:2325-33.

[30] Deganello F, Liotta LF, Longo A, Casaletto MP, Scopelliti M. Cerium effect on the phase structure, phase stability and redox properties of Ce-doped strontium ferrates. J Solid State Chem. 2006;179:3406-19.

[31] Sun Y, Li J, Zeng Y, Amirkhiz BS, Wang M, Behnamian Y, et al. A-site deficient perovskite: the parent for in situ exsolution of highly active, regenerable nano-particles as SOFC anodes. J Mater Chem A. 2015;3:11048-56.

[32] dos Santos-Gómez L, Compana JM, Bruque S, Losilla ER, Marrero-López D. Symmetric electrodes for solid oxide fuel cells based on Zr-doped $SrFeO_{3-\delta}$. Journal of Power Sources. 2015;279:419-27.

[33] Meng X, Liu X, Han D, Wu H, Li J, Zhan Z. Symmetrical solid oxide fuel cells with impregnated $SrFe_{0.75}Mo_{0.25}O_{3-\delta}$ electrodes. Journal of Power Sources. 2014;252:58-63.

[34] Fernandez-Ropero AJ, Porras-Vazquez JM, Cabeza A, Slater PR, Marrero-Lopez D, Losilla ER. High valence transition metal doped strontium ferrites for electrode materials in symmetrical SOFCs. J Power Sources. 2014;249:405-13.

[35] Park S, Vohs JM, Gorte RJ. Direct oxidation of hydrocarbons in a solid-oxide fuel cell. Nature. 2000;404:265-7.

[36] Xiao G, Liu Q, Wang S, Komvokis VG, Amiridis MD, Heyden A, et al. Synthesis and characterization of Mo-doped $SrFeO_{3-\delta}$ as cathode materials for solid oxide fuel cells. Journal of Power Sources. 2012;202:63-9.

[37] Song H, Zhang L, Ozkan US. Investigation of the Reaction Network in Ethanol Steam Reforming over Supported Cobalt Catalysts. Industrial & Engineering Chemistry Research. 2010;49:8984-9.

[38] Ding X, Lv X, Weng Y. Coupling effect of operating parameters on performance of a biogas-fueled solid oxide fuel cell/gas turbine hybrid system. Applied Energy. 2019;254:113675.

[39] Kim T, Liu G, Boaro M, Lee SI, Vohs JM, Gorte RJ, et al. A study of carbon formation and prevention in hydrocarbon-fueled SOFC. Journal of Power Sources. 2006;155:231-8.

[40] Gao J, Hou Z, Guo J, Zhu Y, Zheng X. Catalytic conversion of methane and CO_2 to synthesis gas over a La_2O_3-modified SiO_2 supported Ni catalyst in fluidized-bed reactor. Catalysis Today. 2008;131:278-84.

[41] Zheng Y, Li K, Wang H, Tian D, Wang Y, Zhu X, et al. Designed oxygen carriers from macroporous $LaFeO_3$ supported CeO_2 for chemical-looping reforming of methane. Applied Catalysis B: Environmental. 2017;202:51-63.

[42] Tao S, Irvine JTS. Catalytic Properties of the Perovskite Oxide $La_{0.75}Sr_{0.25}Cr_{0.5}Fe_{0.5}O_{3-\delta}$ in Relation to Its Potential as a Solid Oxide Fuel Cell Anode Material. Chemistry of Materials. 2004;16:4116-21.

[43] Konysheva EY, Xu XX, Irvine JTS. On the existence of A-site deficiency in perovskites and its relation to the electrochemical performance. Advanced Materials (Weinheim, Germany). 2012;24:528-32.

[44] Ben Mya O, dos Santos-Gomez L, Porras-Vazquez JM, Omari M, Ramos-Barrado JR, Marrero-Lopez D. $La_{1-x}Sr_xFe_{0.7}Ni_{0.3}O_{3-\delta}$ as both cathode and anode materials for Solid Oxide Fuel Cells. International Journal of Hydrogen Energy. 2017;42:23160-9.

[45] Du Z, Zhao H, Li S, Zhang Y, Chang X, Xia Q, et al. Exceptionally High Performance Anode Material Based on Lattice Structure Decorated Double Perovskite $Sr_2FeMo_{2/3}Mg_{1/3}O_{6-\delta}$ for Solid Oxide Fuel Cells. Advanced Energy Materials. 2018;8:1800062.

[46] Liu S, Liu Q, Luo J-L. Highly Stable and Efficient Catalyst with In Situ Exsolved Fe–Ni Alloy Nanospheres Socketed on an Oxygen Deficient Perovskite for Direct CO_2 Electrolysis. ACS Catalysis. 2016;6:6219-28.

[47] Goto Y, Taniguchi K, Omata T, Otsuka-Yao-Matsuo S, Ohashi N, Ueda S, et al. Formation of Ni3C Nanocrystals by Thermolysis of Nickel Acetylacetonate in Oleylamine: Characterization Using Hard X-ray Photoelectron Spectroscopy. Chemistry of Materials. 2008;20:4156-60.

[48] Ni C, Carolan D, Rocks C, Hui J, Fang Z, Padmanaban DB, et al. Microplasma-assisted electrochemical synthesis of Co_3O_4 nanoparticles in absolute ethanol for energy applications. Green Chemistry. 2018;20:2101-9.

[49] Niu B, Jin F, Feng T, Zhang L, Zhang Y, He T. A-site deficient $(La_{0.6}Sr_{0.4})_{1-x}Co_{0.2}Fe_{0.6}Nb_{0.2}O_{3-\delta}$ symmetrical electrode materials for solid oxide fuel cells. Electrochimica Acta. 2018;270:174-82.

[50] Armstrong EN, Park J-W, Minh NQ. High-Performance Direct Ethanol Solid Oxide Fuel Cells. Electrochemical and Solid-State Letters. 2012;15:B75.

[51] Meng X, Gong X, Yang N, Yin Y, Tan X, Ma Z-F. Carbon-resistant Ni-YSZ/Cu–CeO_2-YSZ dual-layer hollow fiber anode for micro tubular solid oxide fuel cell. International Journal of Hydrogen Energy. 2014;39:3879-86.

[52] Hsia Y-Y, Huang Y-C, Zheng H-S, Lai Y-L, Hsu Y-J, Luo M-F, et al. Effects of O_2 and H_2O in the Oxidative Steam-Reforming Reaction of Ethanol on Rh Catalysts. The Journal of Physical Chemistry C. 2019;123:11649-61.

[53] Polo-Garzon F, Blum TF, Bao Z, Wang K, Fung V, Huang Z, et al. In Situ Strong Metal–Support Interaction (SMSI) Affects Catalytic Alcohol Conversion. ACS Catalysis. 2021;11:1938-45.

[54] Baruah R, Dixit M, Basarkar P, Parikh D, Bhargav A. Advances in ethanol autothermal reforming. Renewable and Sustainable Energy Reviews. 2015;51:1345-53.

[55] Mattos LV, Jacobs G, Davis BH, Noronha FB. Production of Hydrogen from Ethanol: Review of Reaction Mechanism and Catalyst Deactivation. Chemical Reviews. 2012;112:4094-123.

[56] Laosiripojana N, Assabumrungrat S. The effect of specific surface area on the activity of nano-scale ceria catalysts for methanol decomposition with and without steam at SOFC operating temperatures. Chemical Engineering Science. 2006;61:2540-9.

[57] Baker RTK. Catalytic growth of carbon filaments. Carbon. 1989;27:315-23.

[58] Wang W, Su C, Wu Y, Ran R, Shao Z. Progress in Solid Oxide Fuel Cells with Nickel-Based Anodes Operating on Methane and Related Fuels. Chemical Reviews. 2013;113:8104-51.

[59] Montini T, Melchionna M, Monai M, Fornasiero P. Fundamentals and Catalytic Applications of CeO_2-Based Materials. Chemical Reviews. 2016;116:5987-6041.

[60] Ruiz Puigdollers A, Schlexer P, Tosoni S, Pacchioni G. Increasing Oxide Reducibility: The Role of Metal/Oxide Interfaces in the Formation of Oxygen Vacancies. ACS Catalysis. 2017;7:6493-513.